

# CMOS nanoelectrode array for all-electrical intracellular electrophysiological imaging

Jeffrey Abbott<sup>1‡</sup>, Tianyang Ye<sup>1‡</sup>, Ling Qin<sup>1</sup>, Marsela Jorgolli<sup>2†</sup>, Rona S. Gertner<sup>3</sup>, Donhee Ham<sup>1\*</sup> and Hongkun Park<sup>2,3,4\*</sup>

**Developing a new tool capable of high-precision electrophysiological recording of a large network of electrogenic cells has long been an outstanding challenge in neurobiology and cardiology. Here, we combine nanoscale intracellular electrodes with complementary metal-oxide-semiconductor (CMOS) integrated circuits to realize a high-fidelity all-electrical electrophysiological imager for parallel intracellular recording at the network level. Our CMOS nanoelectrode array has 1,024 recording/stimulation ‘pixels’ equipped with vertical nanoelectrodes, and can simultaneously record intracellular membrane potentials from hundreds of connected *in vitro* neonatal rat ventricular cardiomyocytes. We demonstrate that this network-level intracellular recording capability can be used to examine the effect of pharmaceuticals on the delicate dynamics of a cardiomyocyte network, thus opening up new opportunities in tissue-based pharmacological screening for cardiac and neuronal diseases as well as fundamental studies of electrogenic cells and their networks.**

Within the past decades<sup>1</sup>, optical methods for interrogation using Ca<sup>2+</sup> indicators<sup>2,3</sup>, styryl potentiometric dyes<sup>4,5</sup> and voltage-sensitive proteins<sup>3</sup> have significantly benefited the field of electrophysiology with their ability for massively parallel intracellular recording of membrane potentials of electrogenic cells. Realizing an analogous all-electrical device for electrophysiology—a closely packed electrode array capable of high-precision intracellular recording from a large network of electrogenic cells—has long been a major pursuit in bioengineering, neuro- and cardio-technology<sup>6–14</sup>. These efforts toward all-electrical electrophysiological imaging have led to, most prominently, CMOS microelectrode arrays (MEAs)<sup>15–21</sup> and planar patch-clamp arrays<sup>22–24</sup>. While CMOS MEAs enable massively parallel recording of cellular networks, they are extracellular techniques that do not have the high-sensitivity characteristic of intracellular recording. Microfluidic patch-clamp arrays, on the other hand, allow for high-precision intracellular access, but they are not applicable to network-level interrogation.

In this Article, we report a CMOS nanoelectrode array (CNEA) that bridges the gap between MEAs and patch-clamp arrays and works as a high-fidelity all-electrical electrophysiological imager, performing parallel intracellular recording at the network level. It consists of a tight array of 1,024 recording/stimulation sites or ‘pixels’, with each pixel featuring a set of vertical nanoelectrodes<sup>25–27</sup> operated by the underlying CMOS integrated circuit (IC). We show that the CNEA simultaneously records intracellular membrane potentials of hundreds of connected *in vitro* neonatal rat ventricular cardiomyocytes. We then used it to examine the effect of pharmaceuticals on the fine, important details of the cardiomyocyte network dynamics. The CNEA’s parallel intracellular recording nicely complements that of the optical methods by providing an all-electrical chip-scale interface and label-free operation, while also offering an electrical alternative to optogenetics-based stimulation<sup>28</sup>. It should not only considerably advance high-precision

tissue-based pharmacological screening for cardiac and neuronal diseases<sup>24,26,29–32</sup> but also enable fundamental studies of electrogenic cells and their networks<sup>25,33–35</sup>.

## Circuit and nanoelectrode array

We custom designed the IC using the 0.35- $\mu\text{m}$  CMOS technology (Fig. 1a,b). It contains an array of  $32 \times 32 = 1,024$  pixels with a 126- $\mu\text{m}$  pitch, with each pixel consisting of an amplifier to record electrophysiological events, a stimulator to manipulate membrane potential, and a memory to switch the pixel operation between recording and stimulation (Supplementary Discussion 1 and Supplementary Fig. 1). The IC also includes, outside the pixel array, a global circuitry to control the array operation, such as analog multiplexers for virtually simultaneous readout of all pixels at a sampling rate of 9.75 kHz. Within each pixel, the amplifier and stimulator are connected to a metallic pad on the IC surface (Fig. 1c), on top of which nine vertical nanoelectrodes are post-fabricated using a CMOS-compatible top-down process (Fig. 1d and Supplementary Fig. 2). Each nanoelectrode has a SiO<sub>2</sub> mechanical core, a thin Ti/Pt coating, and SiO<sub>2</sub> insulation at the base. The Ti/Pt tips of the nine electrodes at each pixel are electrically connected together to reduce the overall access impedance into the intracellular matrix<sup>20,25</sup>.

Nanostructures of various geometries—pillars<sup>25,26,36</sup>, tubes<sup>27,37</sup>, kinked triangles<sup>38</sup>, mushrooms<sup>39</sup> and straws<sup>40,41</sup>—have been previously used for intracellularly interfacing with various cell types and at different levels of scalability. The synergy between the nanoelectrodes and the CMOS IC in this work offers critical advances over the previous stand-alone nanoelectrode arrays<sup>25–27,39</sup>, which have been limited to 64 electrodes and simultaneous recording from less than 10 cells<sup>27</sup>. First, the underlying IC allows parallel operation of the large-scale electrode array through on-chip multiplexing, without which the readout of, and wiring to, such a large number of electrodes would be practically impossible<sup>33</sup>. Second, the

<sup>1</sup>School of Engineering and Applied Sciences, Harvard University, Cambridge, Massachusetts 02138, USA. <sup>2</sup>Department of Physics, Harvard University, Cambridge, Massachusetts 02138, USA. <sup>3</sup>Department of Chemistry and Chemical Biology, Harvard University, Cambridge, Massachusetts 02138, USA.

<sup>4</sup>Broad Institute of MIT and Harvard, 415 Main Street, Cambridge, Massachusetts 02142, USA. <sup>†</sup>Present address: Hybrid Modality Engineering R&D, Amgen Inc., 1 Amgen Center Drive, Thousand Oaks, California 91360, USA. <sup>‡</sup>These authors contributed equally to this work. \*e-mail: donhee@seas.harvard.edu; Hongkun\_Park@harvard.edu

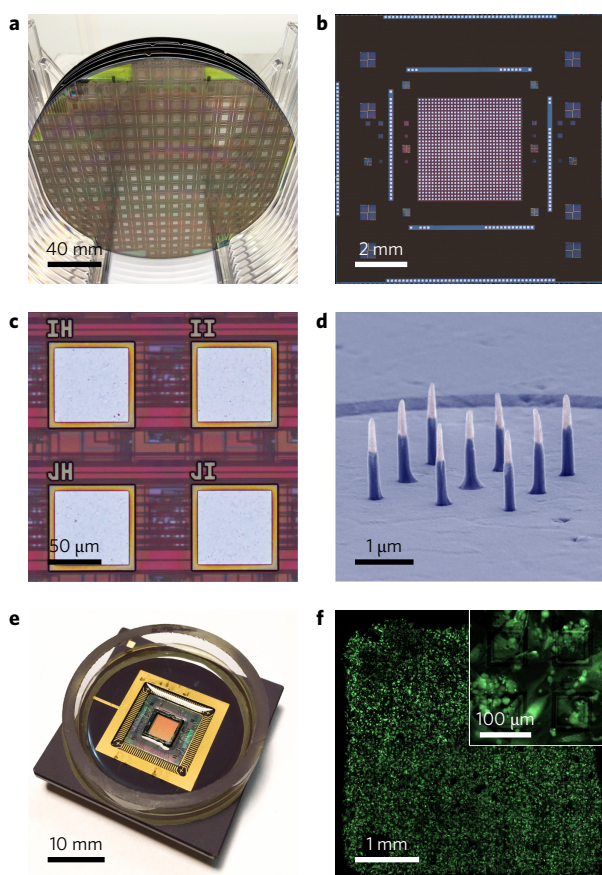


**Figure 1 | CMOS nanoelectrode array (CNEA).** **a**, CMOS ICs on 8 inch wafers fabricated by the 5.0-V 0.35- $\mu\text{m}$  CMOS technology. Each wafer contains 256 ICs. **b**, IC with a  $32 \times 32$  array of pixels at the centre. **c**, Four pixels in the  $32 \times 32$  array. Under each pixel pad lie an amplifier and a memory. **d**, False-coloured scanning electron microscope image of nine vertical nanoelectrodes fabricated per pad. The top of the electrodes has Pt exposed while the base is insulated with  $\text{SiO}_2$ . **e**, The device is wire-bonded to a chip carrier: a glass ring and a polydimethylsiloxane protective layer create a microfluidic well. **f**, Fluorescence image of cardiomyocytes cultured on top of a device (stained with calcein-AM). The inset shows cells on top of four pixel pads. Green colour indicates live cells.

membrane potential signal acquired by the pixel nanoelectrodes is amplified on site by the circuits right underneath, leading to substantial improvements in sensitivity by avoiding a long signal path and resultant attenuation and noise contamination<sup>25</sup>. In fact, since the initial demonstrations of the nanoscale electrodes for electrophysiology, their integration with CMOS electronics has been recognized as a logical next step<sup>8–11,20,25</sup>, but such integration, which entails post-nanofabrication on a CMOS chip and synergic electrical interface design as demonstrated here, has thus far remained to be a substantial technical challenge.

To streamline the amplification of intracellular signals at each pixel, we a.c.-coupled the pixel amplifier (in a bandpass filter configuration) with the nanoelectrodes on top using an on-chip capacitor, and operated the nanoelectrodes in the double-layer capacitive mode<sup>25,42</sup> (Fig. 2a). This arrangement offers two advantages relevant to intracellular recording. First, within the amplifier's passband, which is designed to cover the electrophysiological signal bandwidth (1 Hz–5 kHz; ref. 10), a linear and flat-band gain is established from the intracellular matrix to the amplifier output. Preservation of waveform shape ensured by such a signal amplification path is important because the key aim (and advantage) of intracellular electrodes is the accurate measurements of membrane potentials<sup>26</sup>.

Second, d.c. current is blocked from flowing through the nanoelectrodes, thus minimizing adverse effects on cell viability<sup>25</sup>.

For experiments, the CNEA chip is packaged with a microfluidic well (Fig. 1e and Supplementary Fig. 3) and is plugged into a printed circuit board that interfaces to a computer (Supplementary Fig. 4). The overall capacitance of the nine nanoelectrodes per pad, measured in solution, is  $\sim 1.2$  pF (Supplementary Fig. 5). Measurements of the pixel amplifiers confirm uniform gain across the target frequency range (Fig. 2b) and throughout the  $32 \times 32$  array (Fig. 2c), with an input referred noise of  $\sim 250$   $\mu\text{V}_{\text{rms}}$  (Supplementary Fig. 6) and a pixel power dissipation of 12  $\mu\text{W}$ . Moreover, control experiments with human embryonic kidney (HEK293) cells (a robust model cell line for electrophysiology study) confirmed that the intracellular waveform applied with a patch pipette is faithfully transferred through a coupled cell to the pixel amplifier (Supplementary Fig. 7), thus validating the linear and flat-band gain of the overall nanoelectrode–amplifier chain. Further measurements using the patch clamp allowed for the nanoelectrode/cell interface to be characterized<sup>10,25,27</sup>, with an extracted cell–electrode seal resistance of  $\sim 100$  M $\Omega$  (full range, 15–375 M $\Omega$ ) and access resistance of  $\sim 300$  M $\Omega$  (full range, 40–525 M $\Omega$ ) (Supplementary Discussion 2 and Supplementary Fig. 8). From each pixel's electrical characteristics, such as the passband gain (Fig. 2c) and nanoelectrode conductance (Fig. 2d), we find that  $>90\%$  of the pixels are available for electrophysiological experiments in a typical device. Previous studies have shown that culturing cells on top of nanoelectrodes does not affect cell viability<sup>36</sup>. Consistent with these previous results, fluorescent imaging (Fig. 1f) and electrophysiology experiments show that cells cultured on top of CNEA devices can be interrogated multiple times for up to 7 days (from after 6 days *in vitro* (DIV) up to 13 DIV). Also minimal effects to the nanoelectrodes are observed over multiple uses (Supplementary Fig. 9) with no changes in the performance of the CMOS circuitry.

### Single-cell recording and stimulation

We first tested and optimized the operation of individual CNEA pixels using neonatal rat ventricular cardiomyocytes cultured *in vitro* (Fig. 2e). When a cardiomyocyte sitting on top beats, the pixel nanoelectrodes can readily pick up small extracellular voltage spikes (Fig. 2e, top right). The amplitudes of these extracellular signals are in the range of 250  $\mu\text{V}$ –1.5 mV (Supplementary Fig. 10), much smaller than the action potential measured intracellularly using a patch pipette ( $\sim 120$  mV), but on the same order of typical extracellular signals recorded by planar electrodes<sup>15–21</sup>. To change the operation mode of a CNEA pixel from extracellular to intracellular, we applied an electroporation signal (3 trains of  $5 \times 1.2$  V biphasic pulses at 20 Hz) using the pixel stimulator and made the membrane permeable<sup>25–27</sup> (Fig. 2e, top right). On electroporation, the signal amplitudes measured at the nanoelectrodes jump to  $\sim 5$  mV, suggesting intracellular access. The reduced signal amplitude measured by the nanoelectrode (typically  $\sim 5$  mV but as high as  $\sim 20$  mV) as compared with the patch clamp ( $\sim 120$  mV) is the consequence of (1) the resistive divider between the junctional membrane resistance and seal resistance of the nanoelectrode/cell interface (typically an attenuation of  $\sim 10\times$  but as small as  $2.5\times$ ) and (2) the capacitive divider between the nanoelectrode capacitance, parasitic pad capacitance and amplifier input capacitance (attenuation of  $2.5\times$ ) (Supplementary Discussion 2 and Supplementary Fig. 8). The resistive attenuation of  $2.5$ – $10\times$  is an improvement over previous works<sup>25–27</sup> (the attenuation could be further lessened by increasing the seal resistance to the level comparable to the conventional patch pipette; such improvement of the cell-to-electrode interface is an active subject of study but, as of yet, a significant challenge in nanoelectrode-based electrophysiology<sup>20,27,39</sup>). Furthermore, the measured

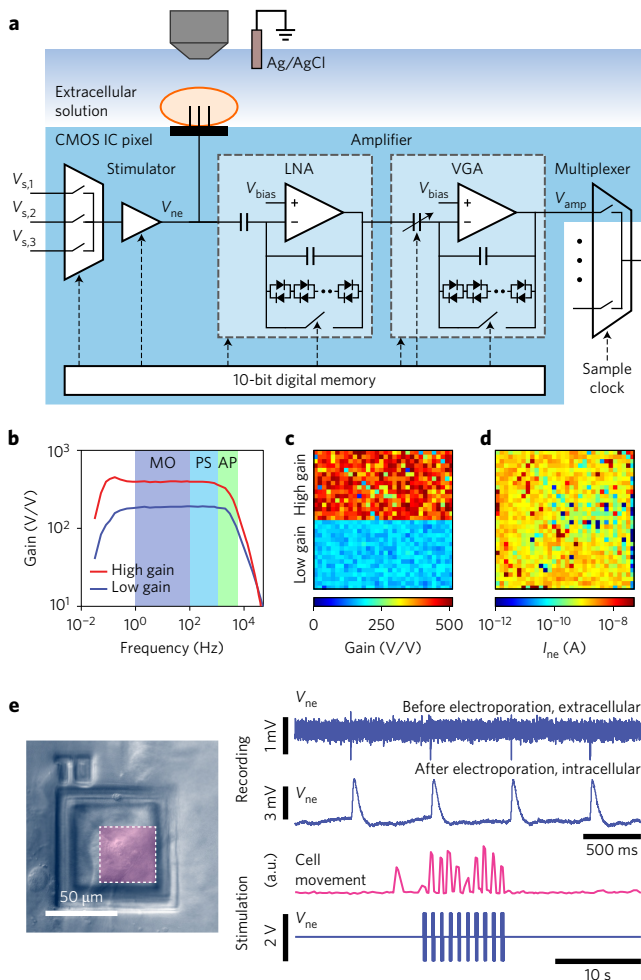


**Figure 2 | CNEA pixel function and recording of a single rat neonatal ventricular cardiomyocyte.** **a**, Schematic of an individual pixel circuit with a cell on top. Three major building blocks of each pixel are a stimulator, an amplifier consisting of a first-stage low noise amplifier (LNA) and a second-stage variable gain amplifier (VGA), and a 10-bit digital memory. The stimulator uses a 3:1 MUX to choose from three possible input voltages ( $V_{s,1-3}$ ) and the amplifier requires a low noise bias voltage,  $V_{bias}$ , to set the DC output (Supplementary Information). **b**, Measured amplifier transfer function (the ratio of the amplifier output voltage,  $V_{amp}$ , to the nano-electrode voltage,  $V_{ne}$ ) at maximum gain of the two types of amplifier (high gain/low gain). These two amplifier configurations are implemented to explore design tradeoffs (Supplementary Discussion 1). Typical bandwidths of membrane oscillations (MO), postsynaptic potentials (PS) and neuronal action potentials (AP) are juxtaposed<sup>10</sup>. **c**, Heat map of maximum gain at 100 Hz across an array. The top half amplifier design exhibits a maximum gain of  $\sim 375$  V/V while the bottom half demonstrates  $\sim 150$  V/V due to design tradeoffs. **d**, Heat map of nano-electrode currents,  $I_{ne}$ , across an array at 1.5 V versus Ag/AgCl reference electrode. From these current measurements, we can determine the pixels suitable for electrophysiology experiments: a small number of pixels with nano-electrode currents less than  $\sim 30$  pA are deemed as non-operative. **e**, Left: differential interference contrast microscope image of an isolated cardiomyocyte sitting on top of the nano-electrodes on a CNEA pixel pad. Top right: extracellular and intracellular recordings of cardiac action potentials from the same cardiomyocyte before and after electroporation. Bottom right: stimulation of a cardiomyocyte using a biphasic voltage pulse sequence with synchronized cell movement analysed from video differentials.

waveforms resemble those of patch pipettes, consistent with their intracellular nature<sup>43</sup>. The addition of blebbistatin ( $3 \mu\text{M}$ ), which decouples mechanical beating from the action potential, does not

change the measured signal, verifying its electrical origin. In addition to using an amplifier of a CNEA pixel for membrane potential recording, we can use the pixel's stimulator to induce the action potential of a cardiomyocyte: for instance, by applying a biphasic voltage pulse sequence every 1 s through a pixel stimulator, we can change the beating frequency of a cardiomyocyte from  $\sim 1/20$  to 1 Hz (Fig. 2e, bottom right and Supplementary Movie 1).

### Network-level interrogation and manipulation

Following this single-cell recording and stimulation, we demonstrated the network-level intracellular recording capability of our CNEA using a tightly connected *in vitro* cultured cardiomyocyte sheet. Because extracellular access is readily available to the CNEA before electroporation, however, we start with network-level extracellular recording. In the example shown in Fig. 3a (leftmost panel), we find that 968 pixels are extracellularly coupled to cardiomyocytes after time-aligned averaging (see Supplementary Methods). By following the action potential firing times of these extracellularly coupled cells, we can determine that the cardiomyocyte sheet exhibits spatially homogenous action potential propagation (starting upper right and propagating radially) with a conduction velocity of  $9 \text{ cm s}^{-1}$  (Supplementary Fig. 11).

We subsequently changed the CNEA operation into the intracellular mode by applying simultaneous electroporation pulses across all pixels. We initially observed a spiral pattern of action potential propagation around the periphery with a conduction velocity of  $2 \text{ cm s}^{-1}$  (Fig. 3a, at 23.3 s, Supplementary Fig. 12). As time elapsed, however, we started to record the intracellular signals from cells at the central part of the cardiomyocyte sheet as well (Supplementary Movie 2), and the number of intracellularly recorded cells increased to 235 at 48.3 s after electroporation.

The expansion of the intracellularly recorded region from the sheet periphery into the centre (Fig. 3a) is likely due to the fact that right after electroporation, the large number of cells at the centre are leaking currents and thus fail to fire action potentials reliably. With time, the cellular membranes start to form tight seals around nano-electrodes, and the cells at the centre regain their normal function, resulting in intracellular coupling to CNEA pixels (Fig. 3a, at 43.6 s and 48.3 s). The propagation pattern and the conduction velocity of action potentials then return to their original, pre-electroporation, values within a few minutes (Fig. 3a, at 173.3 s), indicating that over time the cardiomyocyte sheet recovers from initial shock after electroporation.

The action potential dynamics of a cardiomyocyte sheet is sensitively dependent on the perturbation that we apply with the CNEA pixels. In the cardiomyocyte sheet presented in Fig. 3a, in which the entire CNEA is used to electroporate the sheet, the action potential propagation pattern changes from spiral to spatially homogeneous as time lapses. When we reduced the size of the electroporation region by covering  $\sim 6$  peripheral rows of pixels with polydimethylsiloxane, however, the behaviour of a cardiomyocyte sheet changed dramatically: as seen from Fig. 3b and Supplementary Movie 3, the cardiomyocyte sheet exhibits consistent reentrant behaviour (frequency of  $\sim 5$  Hz) for  $\sim 50$  s, totaling more than 250 sustained cycles. This leakage-induced reentry behaviour is similar to that observed in stem cell/cardiomyocyte<sup>44</sup> and fibroblast/cardiomyocyte co-cultures<sup>45</sup> where the passive stem cells or fibroblasts, which form gap junctions with the cardiomyocytes, cause increased electrical loading. In our example, electroporation-induced leakage plays the role of electrical loading. The examples presented in Fig. 3a,b clearly illustrate the potential of the CNEA in manipulating and engineering cardiomyocyte network characteristics via stimulation/electroporation.

The data in Fig. 3c show the detailed characterization of cell-electrode coupling. In general, the number of intracellularly coupled cells decreases over time (for example, from 235 at 48.3 s

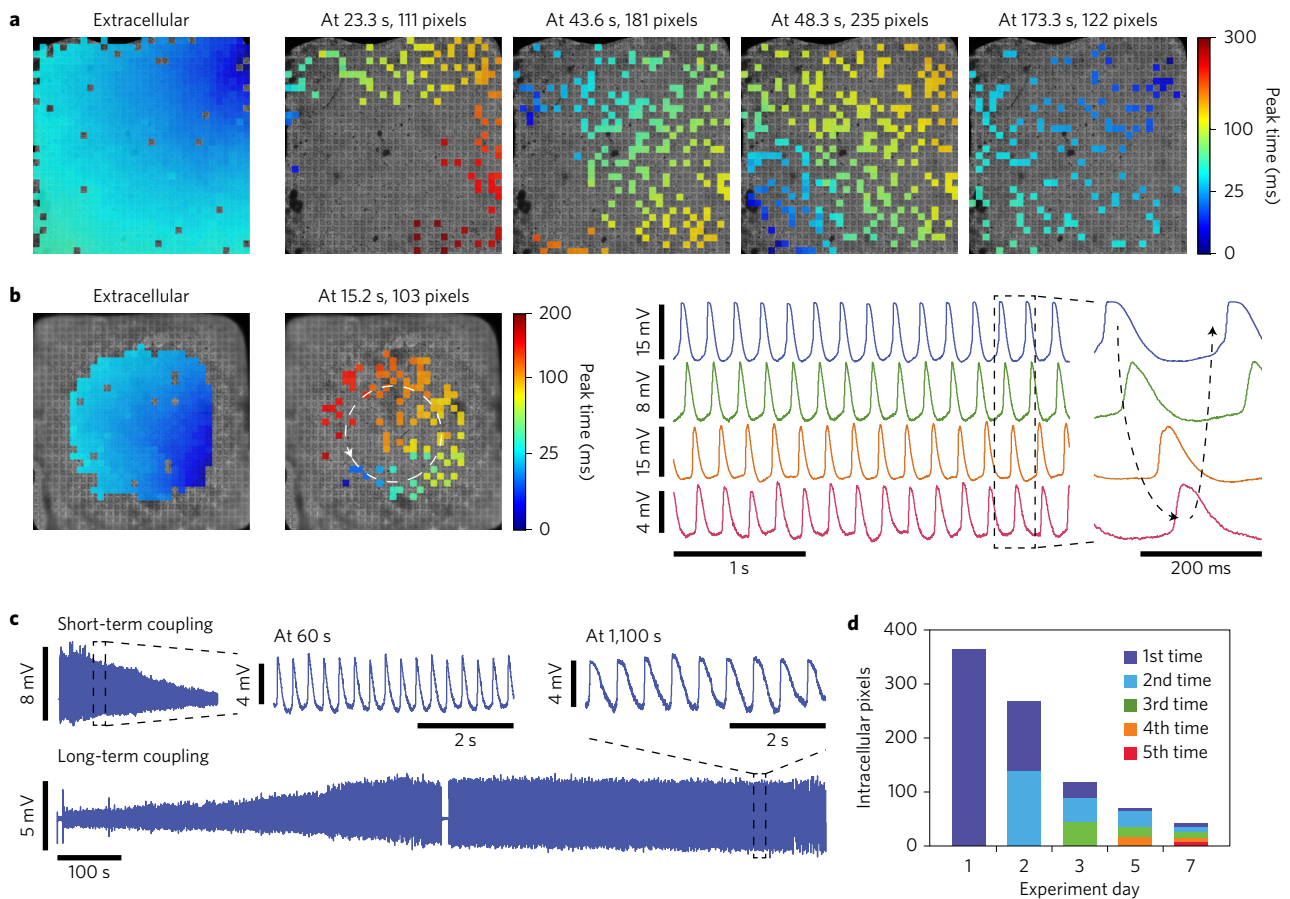


**Figure 3 | Network-level intracellular recording of *in vitro* neonatal rat ventricular cardiomyocyte cultures.** **a**, Mapping of action potential propagation patterns across the array at different time points before and after electroporation. An extracellular recording before electroporation shows homogeneous action potential propagation, whereas intracellular recordings after electroporation show an evolution from spiral propagation at 23.3 s and 43.6 s back to homogeneous propagation at 48.3 s and 173.3 s. **b**, To promote reentrant propagation, the nanoelectrode array is reduced in size by covering ~6 peripheral rows of pixels with polydimethylsiloxane and rounding; extracellular action potential mapping before electroporation shows homogenous propagation through the sheet. After electroporation, intracellular recordings reveal a marked reduction in conduction velocity and spiral reentrant behaviour (indicated by the white dashed arrow on the map). Representative recordings from cardiomyocytes approximately 90° out of phase show the sustained oscillations at 5 Hz (indicated with the black dashed arrows); the pattern is sustained for ~50 s for ~250 cycles. **c**, Representative cardiomyocyte recordings, referred to  $V_{ne}$ , of short-term coupling for ~5 min and long-term coupling for more than 20 min (recording re-started after a 10 s delay midway). **d**, Number of cells intracellularly measured in 5 experiments over 7 days. The number of times the cells were measured are indicated by the different colours.

to 122 at 173.3 s in Fig. 3a) because the metallic tips get expelled out of some of the cells with time<sup>26,27</sup>. Such ejection of electrodes is manifested by diminishing signal amplitude (Fig. 3c, top). Some pixels exhibit prolonged intracellular coupling (Fig. 3c, bottom), however, indicating the cell-to-cell variation of the tip/membrane interface. Extended recording studies show that we can perform repeated intracellular measurements on multiple days (Fig. 3d). Overall, we find that, in a typical CNEA device with a cardiomyocyte sheet, >30% of the pixels can get intracellularly coupled at least once over the recording time.

### Investigation of drug responses of cardiac tissue

The CNEA’s capabilities demonstrated above can benefit several areas of cardiology, such as fundamental studies of signal propagation and tissue-based drug screening for cardiac diseases<sup>26,29–32,46</sup>. In the example shown in Fig. 4, we investigated the effects of various drugs on cardiomyocyte sheets using the CNEA. For the measurements of simple variables of cardiac dynamics, such as the beat frequency and conduction velocity, we can operate the CNEA in the extracellular mode like traditional MEAs. For example, the CNEA extracellularly measures the increase in beat frequency on the application of norepinephrine (Fig. 4a)

and the decrease in conduction velocity under the influence of 1-heptanol (a known gap-junction blocker<sup>46</sup>; Fig. 4b).

In addition to these extracellular measurements, however, the CNEA operating in the intracellular mode can determine, with high precision, the duration and shape of membrane potentials as well as their propagation dynamics. These capabilities, which are afforded by intracellular access, represent the clearest advantages of the CNEA over traditional MEAs in studying the network dynamics and examining the drug effect. Figure 4c,d illustrate one specific example measured at the single-pixel level: significant elongation of action potential durations (APDs) on the application of ATX-II (50 nM) that is recorded by a CNEA pixel operating in the intracellular mode. ATX-II is a  $Na^+$  ion channel toxin known to cause a delayed inactivation of the fast  $Na_v1.5$  channel, thus mimicking the effects of genetic mutations of *SCN5A* responsible for congenital long-QT syndrome type 3<sup>47</sup>. The behaviours in Fig. 4c,d are consistent with this known effect, and accurately reproduce previous patch-pipette measurements<sup>47</sup>. The CNEA also measures the subsequent reversal of the actions of ATX-II by ranolazine<sup>47</sup> (10  $\mu$ M) (Fig. 4c,d). We note that the ability to investigate these types of drug effect is essential for preclinical development of pharmaceutical candidates because drug-induced

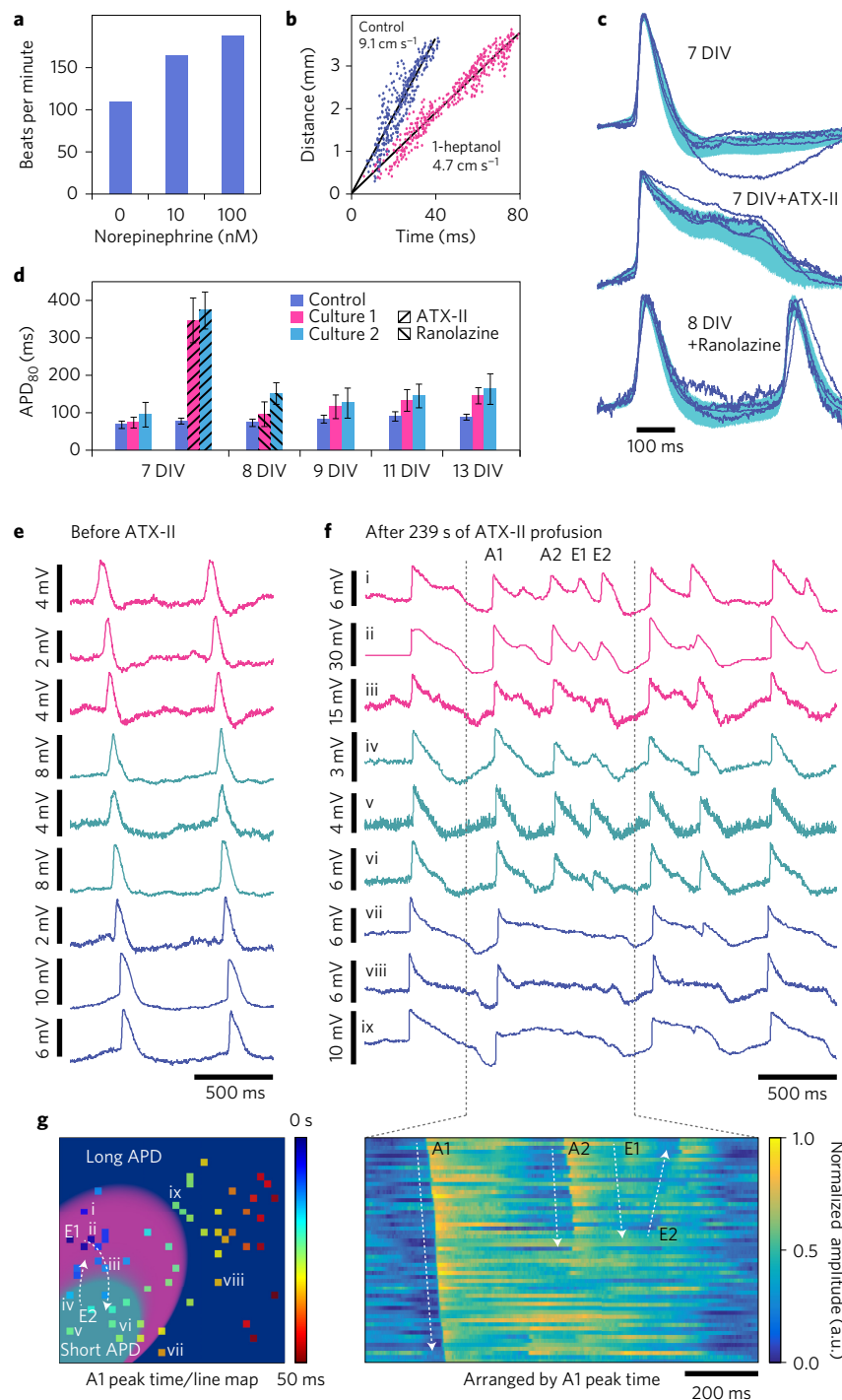


**Figure 4 | CNEA study of effects of various drugs on *in vitro* neonatal rat ventricular cardiomyocyte cultures.** **a**, Extracellular measurements of the beat frequency before and after the application of norepinephrine (10 nM and 100 nM). **b**, The linear fit of extracellular peak times before and after the addition of 1-heptanol (1 mM), showing a 51% reduction in conduction velocity. **c**, Averaged and amplitude-normalized action potential waveforms (measured as  $V_{ne}$ ) before and after the application of ATX-II (50 nM) for five different pixels 7 days after *in vitro* culture (DIV). Incubation with ranolazine (10  $\mu$ M) brings the waveform back on the next day (8 DIV). The shaded envelopes indicate the standard deviation of all coupled pixel recordings; signal averaging was performed to increase the sample size of the action potential waveform shape. **d**, Action potential duration (APD) at 80% repolarization (APD<sub>80</sub>) for a control culture and two test cultures over 6 experiment days with the application of ATX-II (50 nM) at 7 DIV followed by one-day incubation of ranolazine (10  $\mu$ M). Error bars represent standard deviation. **e, f**, Representative recordings, referred to  $V_{ne}$ , before (**e**) and after (**f**) ATX-II application for culture 1 shows significant action potential widening (including peaks A1, A2) and early afterdepolarizations (EADs) (peaks E1, E2). **g**, Spatial distribution of 54 pixels (left) and their voltage traces (right). The traces were recorded in the denoted time period shown in (**f**). Traces are arranged vertically in the voltage trace plot (right) and coloured in the spatial map (left) based on the peak time of A1. Traces i-ix in (**f**) are also labelled on the map. The background colours on the map (left) denote regions with long APD (blue), short APD (green) and a transitional region (magenta); E1 and E2 originate and propagate at the interface indicated with the white dashed arrows. The voltage trace plot (right) clearly shows the action potential (A1, A2) and EAD (E1, E2) propagation, indicated with the white dashed arrows, in the short APD region (top half) and long APD region (bottom half).

pro-arrhythmia is the most common cause of withdrawal or restriction of marketed drugs<sup>30</sup>.

Beyond the single-pixel intracellular recording, the true power of the CNEA's network-level intracellular recording capability is best illustrated by high-precision examination of drug effects on the network dynamics. Figure 4e–g show the use of the CNEA to map the propagation of action potentials and subthreshold events in an *in vitro* cardiomyocyte sheet under ATX-II (see also Supplementary Movie 4). At 239 s after ATX-II perfusion, the cells across the sheet exhibit constant increase in APDs but with differing degrees of APD elongation depending on the regions (Fig. 4e–g): the cells in the lower left (for example, pixels iv–vi) and right half (for example, pixels vii–ix) exhibit distinctly shorter and longer APDs, respectively, with a transition region (for example, pixels i–iii) in between (Fig. 4g).

The CNEA recording further reveals that this spatial APD inhomogeneity is linked to local polarization dynamics and their spatial correlations. First, the cells in the transition region fire a second action potential (A2) quickly after the first action potential (A1). This second action potential propagates to the short APD region, but does not reach the long APD region because the cells in that region are too depolarized to fire an additional action potential. This marks the onset of an arrhythmia within the cardiomyocyte sheet.

Second, the cells in the transition APD region exhibit an early afterdepolarization (EAD: small membrane depolarization that occurs before the membrane completely repolarizes from the action potential) (E1) after the second action potential (A2), which then propagates to the cells in the short APD region to cause triggered activity (TA)<sup>48</sup>. This TA propagates back to the cells in the transition APD region yet again, causing a second EAD (E2) in the transition region (Fig. 4f,g). Once again, the long APD region with an extended depolarization period is not involved in these local dynamics. The origination of the TA by the EAD (E1), and the slower propagation of the TA-induced EAD (E2, Supplementary Fig. 13)—all revealed by the CNEA recording in Fig. 4—are consistent with what have been observed previously in cardiac tissues with arrhythmias using voltage-sensitive dyes<sup>48,49</sup>. Importantly, the recording of these subthreshold membrane potential dynamics across a cellular network has not been possible with traditional electrophysiological tools such as patch pipettes or extracellular MEAs. As such, the measurements presented in Fig. 4 accentuate the CNEA's ability to both analyse intracellular subthreshold events in individual cells and track network dynamics across a large number of cells, highlighting the promise of the CNEA for tissue-based pharmaceutical drug screening.

## Conclusion

The present study represents the first all-electrical demonstration of high-precision network-level electrophysiology, which is made possible by combining the intracellular capability of nanoelectrodes with the scalability of the CMOS IC technology. Moving beyond this prototype implementation with 1,024 recording/stimulation pixels, it should be relatively straightforward to implement a much larger number of pixels and a smaller pitch size by harnessing advances in CMOS fabrication. Moreover, with further refinements in nano/bio interfaces and cell/tissue culture protocols, the CNEA can be extended to *in vitro* neuron cultures and tissue preparations for functional connectome mapping or network-level manipulations. As such, this study opens up an exciting new vista in fundamental studies of electrogenic cells and their networks as well as high-precision pharmacological screening for cardiac and neuronal diseases.

## Methods

Methods and any associated references are available in the [online version of the paper](#).

Received 15 March 2016; accepted 6 January 2017;  
published online 13 February 2017

## References

- Herron, T. J., Lee, P. & Jalife, J. Optical imaging of voltage and calcium in cardiac cells & tissues. *Circ. Res.* **110**, 609–623 (2012).
- Cheng, H., Lederer, W. J. & Cannell, M. B. Calcium sparks: elementary events underlying excitation-contraction coupling in heart muscle. *Science* **262**, 740–744 (1993).
- Hou, J. H., Kralj, J. M., Douglass, A. D., Engert, F. & Cohen, A. E. Simultaneous mapping of membrane voltage and calcium in zebrafish heart *in vivo* reveals chamber-specific developmental transitions in ionic currents. *Front. Physiol.* **5**, 344 (2014).
- Matiukas, A. *et al.* New near-infrared optical probes of cardiac electrical activity. *Am. J. Physiol. Heart Circ. Physiol.* **290**, H2633–H2643 (2006).
- Matiukas, A. *et al.* Near-infrared voltage-sensitive fluorescent dyes optimized for optical mapping in blood-perfused myocardium. *Heart Rhythm* **4**, 1441–1451 (2007).
- Fromherz, P. Electrical interfacing of nerve cells and semiconductor chips. *ChemPhysChem* **3**, 276–284 (2002).
- Alivisatos, A. P. *et al.* The brain activity map. *Science* **339**, 1284–1285 (2013).
- Angle, M. R., Cui, B. & Melosh, N. A. Nanotechnology and neurophysiology. *Curr. Opin. Neurobiol.* **32**, 132–140 (2015).
- Robinson, J. T., Jorgolli, M. & Park, H. Nanowire electrodes for high-density stimulation and measurement of neural circuits. *Front. Neural Circuits* **7**, 38 (2013).
- Spira, M. E. & Hai, A. Multi-electrode array technologies for neuroscience and cardiology. *Nature Nanotech.* **8**, 83–94 (2013).
- Alivisatos, A. P. *et al.* Nanotools for neuroscience and brain activity mapping. *ACS Nano* **7**, 1850–1866 (2013).
- Viventi, J. *et al.* A conformal, bio-interfaced class of silicon electronics for mapping cardiac electrophysiology. *Sci. Transl. Med.* **2**, 24ra22 (2010).
- Viventi, J. *et al.* Flexible, foldable, actively multiplexed, high-density electrode array for mapping brain activity *in vivo*. *Nat. Neurosci.* **14**, 1599–1605 (2011).
- Kodandaramaiah, S. B., Franzesi, G. T., Chow, B. Y., Boyden, E. S. & Forest, C. R. Automated whole-cell patch-clamp electrophysiology of neurons *in vivo*. *Nat. Methods* **9**, 585–587 (2012).
- Eversmann, B. *et al.* A 128 × 128 CMOS biosensor array for extracellular recording of neural activity. *IEEE J. Solid-State Circuits* **38**, 2306–2317 (2003).
- Heer, F. *et al.* CMOS microelectrode array for bidirectional interaction with neuronal networks. *IEEE J. Solid-State Circuits* **41**, 1620–1629 (2006).
- Berdondini, L. *et al.* Active pixel sensor array for high spatio-temporal resolution electrophysiological recordings from single cell to large scale neuronal networks. *Lab Chip* **9**, 2644 (2009).
- Frey, U. *et al.* Switch-matrix-based high-density microelectrode array in CMOS technology. *IEEE J. Solid-State Circuits* **45**, 467–482 (2010).
- Huys, R. *et al.* Single-cell recording and stimulation with a 16k micro-nail electrode array integrated on a 0.18 μm CMOS chip. *Lab Chip* **12**, 1274–1280 (2012).
- Sileo, L. *et al.* Electrical coupling of mammalian neurons to microelectrodes with 3D nanoprotusions. *Microelectron. Eng.* **111**, 384–390 (2013).
- Tsai, D., John, E., Chari, T., Yuste, R. & Shepard, K. High-channel-count, high-density microelectrode array for closed-loop investigation of neuronal networks. *Proc. Annu. Int. Conf. IEEE Eng. Med. Biol. Soc. EMBS* 7510–7513 (2015).
- Fertig, N., Blick, R. H. & Behrends, J. C. Whole cell patch clamp recording performed on a planar glass chip. *Biophys. J.* **82**, 3056–3062 (2002).
- Lau, A. Y., Hung, P. J., Wu, A. R. & Lee, L. P. Open-access microfluidic patch-clamp array with raised lateral cell trapping sites. *Lab Chip* **6**, 1510–1515 (2006).
- Dunlop, J., Bowlby, M., Peri, R., Vasilyev, D. & Arias, R. High-throughput electrophysiology: an emerging paradigm for ion-channel screening and physiology. *Nat. Rev. Drug Discov.* **7**, 358–368 (2008).
- Robinson, J. T. *et al.* Vertical nanowire electrode arrays as a scalable platform for intracellular interfacing to neuronal circuits. *Nat. Nanotech.* **7**, 180–184 (2012).
- Xie, C., Lin, Z., Hanson, L., Cui, Y. & Cui, B. Intracellular recording of action potentials by nanopillar electroporation. *Nat. Nanotech.* **7**, 185–190 (2012).
- Lin, Z. C., Xie, C., Osakada, Y., Cui, Y. & Cui, B. Iridium oxide nanotube electrodes for sensitive and prolonged intracellular measurement of action potentials. *Nat. Commun.* **5**, 3206 (2014).
- Hochbaum, D. R. *et al.* All-optical electrophysiology in mammalian neurons using engineered microbial rhodopsins. *Nat. Methods* **11**, 825–833 (2014).
- Navarrete, E. G. *et al.* Screening drug-induced arrhythmia using human induced pluripotent stem cell-derived cardiomyocytes and low-impedance microelectrode arrays. *Circulation* **128**, S3–S13 (2013).
- Kannankeril, P. J. & Roden, D. M. Drug-induced long QT and torsade de pointes: recent advances. *Curr. Opin. Cardiol.* **22**, 39–43 (2007).
- Stett, A. *et al.* Biological application of microelectrode arrays in drug discovery and basic research. *Anal. Bioanal. Chem.* **377**, 486–495 (2003).
- Itzhaki, I. *et al.* Modelling the long QT syndrome with induced pluripotent stem cells. *Nature* **471**, 225–229 (2011).

33. Buzsáki, G. Large-scale recording of neuronal ensembles. *Nat. Neurosci.* **7**, 446–451 (2004).
34. Gollisch, T. & Meister, M. Eye smarter than scientists believed: neural computations in circuits of the retina. *Neuron* **65**, 150–164 (2010).
35. Yuste, R. From the neuron doctrine to neural networks. *Nat. Rev. Neurosci.* **16**, 487–497 (2015).
36. Shalek, A. K. *et al.* Vertical silicon nanowires as a universal platform for delivering biomolecules into living cells. *Proc. Natl Acad. Sci. USA* **107**, 1870–1875 (2010).
37. Duan, X. *et al.* Intracellular recordings of action potentials by an extracellular nanoscale field-effect transistor. *Nat. Nanotech.* **7**, 174–179 (2011).
38. Tian, B. *et al.* Three-dimensional, flexible nanoscale field-effect transistors as localized bioprobes. *Science* **329**, 830–834 (2010).
39. Hai, A., Shappir, J. & Spira, M. E. In-cell recordings by extracellular microelectrodes. *Nat. Methods* **7**, 200–202 (2010).
40. Vandersarl, J. J., Xu, A. M. & Melosh, N. A. Nanostraws for direct fluidic intracellular access. *Nano Lett.* **12**, 3881–3886 (2012).
41. Xie, X. *et al.* Nanostraw-electroporation system for highly efficient intracellular delivery and transfection. *ACS Nano* **7**, 4351–4358 (2013).
42. Franks, W., Schenker, I., Schmutz, P. & Hierlemann, A. Impedance characterization and modelling of electrodes for biomedical applications. *IEEE Trans. Biomed. Eng.* **52**, 1295–1302 (2005).
43. Varró, A., Lathrop, D. A., Hester, S. B., Nánási, P. & Papp, J. G. Ionic currents and action potentials in rabbit, rat, and guinea pig ventricular myocytes. *Basic Res. Cardiol.* **2**, 93–102 (1993).
44. Chang, M. G. *et al.* Proarrhythmic potential of mesenchymal stem cell transplantation revealed in an in vitro coculture model. *Circulation* **113**, 1832–1841 (2006).
45. Yue, L., Xie, J. & Nattel, S. Molecular determinants of cardiac fibroblast electrical function and therapeutic implications for atrial fibrillation. *Cardiovasc. Res.* **89**, 744–753 (2011).
46. Natarajan, A. *et al.* Patterned cardiomyocytes on microelectrode arrays as a functional, high information content drug screening platform. *Biomaterials* **32**, 4267–4274 (2011).
47. Shryock, J. C., Song, Y., Rajamani, S., Antzelevitch, C. & Belardinelli, L. The arrhythmogenic consequences of increasing late  $I_{Na}$  in the cardiomyocyte. *Cardiovasc. Res.* **99**, 600–611 (2013).
48. Maruyama, M. *et al.* Genesis of phase 3 early afterdepolarizations and triggered activity in acquired long-QT syndrome. *Circ. Arrhythmia Electrophysiol.* **4**, 103–111 (2011).
49. Chang, M. G. *et al.* Bi-stable wave propagation and early afterdepolarization-mediated cardiac arrhythmias. *Heart Rhythm* **9**, 115–122 (2012).

### Acknowledgements

The authors thank J. MacArthur, G. Zhong, D. Ha, B. Tinner and B. VanderElzen for scientific discussions and technical assistance. The CNEA post-fabrication and characterization were performed, in part, at the Center for Nanoscale Systems at Harvard University. The authors are grateful for the support of this research by Catalyst foundation, Valhalla, New York (J.A., D.H. and H.P.), the Army Research Office (W911NF-15-1-0565 to D.H.), the National Institutes of Health (1-U01-MH105960-01 to H.P.), the Gordon and Betty Moore Foundation (to H.P.), and the US Army Research Laboratory and the US Army Research Office (W911NF1510548 to H.P.).

### Author contributions

H.P., D.H., J.A., T.Y., L.Q. and M.J. conceived and designed the experiments. J.A. and L.Q. designed the CMOS IC, and T.Y. and M.J. performed post-fabrication of nanoelectrodes. J.A., T.Y., M.J. and R.S.G. performed the experiments, and J.A., T.Y., D.H. and H.P. analysed the data. H.P. and D.H. supervised the project. J.A., T.Y., D.H. and H.P. wrote the manuscript, and all authors read and discussed it.

### Additional information

Supplementary information is available in the [online version of the paper](#). Reprints and permissions information is available online at [www.nature.com/reprints](http://www.nature.com/reprints). Correspondence and requests for materials should be addressed to D.H. and H.P.

### Competing financial interests

The authors declare no competing financial interests.

## Methods

The vertical nanoelectrodes were fabricated using a modified process from previous work<sup>25</sup> to meet the temperature requirements of the CMOS IC (Supplementary Fig. 2). The IC was wire-bonded onto a chip carrier (Spectrum Semiconductor Material) and packaged with polydimethylsiloxane for cell culture (Supplementary Fig. 3). Neonatal rat ventricular cardiomyocytes were obtained from QBM Cell Science, and electrophysiology

experiments were performed 5–14 days after plating at 37 °C in culture media. Intracellular waveforms were filtered from 1 to 500 Hz, whereas extracellular waveforms were high-pass filtered using a 300 Hz pole. All pharmaceutical materials were obtained from Sigma Aldrich. Full Methods are provided in the Supplementary Information.

**Data availability.** All relevant data are available from the authors.